Published in final edited form as:
J Nucl Med. 2008 April ; 49(4): 667–673. doi:10.2967/jnumed.107.040576.

Imaging of VEGF Receptor in a Rat Myocardial Infarction Model Using PET

Martin Rodriguez-Porcel[1,2], **Weibo Cai**[1], **Olivier Gheysens**[1], **Jürgen K. Willmann**[1], **Kai Chen**[1], **Hui Wang**[1], **Ian Y. Chen**[1,3], **Lina He**[1], **Joseph C. Wu**[1,4], **Zi-bo Li**[1], **Khalid A. Mohamedali**[5], **Sehoon Kim**[5], **Michael G. Rosenblum**[5], **Xiaoyuan Chen**[1], and **Sanjiv Sam Gambhir**[1,3]

[1]Molecular Imaging Program at Stanford (MIPS), Department of Radiology, Division of Nuclear Medicine, Stanford University, Stanford, California

[2]Division of Cardiovascular Diseases, Department of Internal Medicine, Mayo Clinic College of Medicine, Rochester, Minnesota

[3]Department of Bioengineering, Stanford University, Stanford, California

[4]Department of Cardiology, Stanford University, Stanford, California

[5]Department of Experimental Therapeutics, M.D. Anderson Cancer Center, Houston, Texas

Abstract

Myocardial infarction (MI) leads to left ventricular (LV) remodeling, which leads to the activation of growth factors such as vascular endothelial growth factor (VEGF). However, the kinetics of a growth factor's receptor expression, such as VEGF, in the living subject has not yet been described. We have developed a PET tracer (^{64}Cu-DOTA-VEGF$_{121}$ [DOTA is 1,4,7,10-tetraazadodecane-*N*,*N*′,*N*″,*N*‴-tetraacetic acid]) to image VEGF receptor (VEGFR) expression after MI in the living subject.

Methods—In Sprague–Dawley rats, MI was induced by ligation of the left coronary artery and confirmed by ultrasound (n = 8). To image and study the kinetics of VEGFRs, ^{64}Cu-DOTA-VEGF$_{121}$ PET scans were performed before MI induction (baseline) and on days 3, 10, 17, and 24 after MI. Sham-operated animals served as controls (n = 3).

Results—Myocardial origin of the ^{64}Cu-DOTA-VEGF$_{121}$ signal was confirmed by CT coregistration and autoradiography. VEGFR specificity of the ^{64}Cu-DOTA-VEGF$_{121}$ probe was confirmed by in vivo use of a ^{64}Cu-DOTA-VEGF$_{mutant}$. Baseline myocardial uptake of ^{64}Cu-DOTA-VEGF$_{121}$ was minimal (0.30 ± 0.07 %ID/g [percentage injected dose per gram of tissue]); it increased significantly after MI (day 3, 0.97 ± 0.05 %ID/g; $P < 0.05$ vs. baseline) and remained elevated for 2 wk (up to day 17 after MI), after which time it returned to baseline levels.

Conclusion—We demonstrate the feasibility of imaging VEGFRs in the myocardium. In summary, we imaged and described the kinetics of ^{64}Cu-DOTA-VEGF$_{121}$ uptake in a rat model of MI. Studies such as the one presented here will likely play a major role when studying pathophysiology and assessing therapies in different animal models of disease and, potentially, in patients.

For correspondence or reprints contact: Sanjiv Sam Gambhir, MD, PhD, Stanford University School of Medicine, Bio-X Program, Departments of Radiology and Bioengineering, The James H. Clark Center, 318 Campus Dr., Clark E150, Stanford, CA 94305-5427. sgambhir@stanford.edu.

Keywords

myocardial infarction; angiogenesis; vascular endothelial growth factor (VEGF); VEGF receptor (VEGFR); PET; ^{64}Cu

Myocardial infarction (MI), one of the most significant consequences of coronary artery disease (CAD), leads to an upregulation of different growth factors (1,2) that can lead to tissue remodeling. Vascular endothelial growth factor (VEGF) is the most prominent member of a family of growth factors that has been strongly associated with angiogenic stimuli in different pathophysiologic situations (3–8) and likely plays a role in left ventricular (LV) remodeling after MI. Previous studies have shown that MI leads to an initial increase in the expression of VEGF and subsequent increase in the expression of the VEGF receptors (VEGFRs) (1,9).

Currently, most of the information we have with regard to biologic pathways involved in myocardial LV remodeling after MI derives from ex vivo tissue analysis (1,2,9). Study of biologic pathways in the living subject would permit a more physiologic assessment of these pathways as well as longitudinal monitoring of changes that may occur. However, until recently, it was not possible to assess biologic pathways in the living subject. Advances in the development of molecular imaging probes have allowed scientists to start addressing these questions (10–12). Recently, efforts have been made to develop new probes to image and study biologic pathways in the living subject after MI. Using molecular imaging strategies, investigators have shown that after MI there is an upregulation of matrix metalloproteinases (MMPs), in particular MMP-2 and MMP-9 (13,14). Furthermore, significant efforts have been made to image some of the effects of LV remodeling after MI, such as myocardial neovascularization. Specifically, Meoli et al. have demonstrated an increased expression of $\alpha_v\beta_3$ integrin (a transmembrane protein that is only expressed in newly formed vessels) after MI (15). In addition, using ^{111}In-VEGF$_{121}$, Lu et al. showed an increase in VEGF expression in ischemic muscle (16). However, the biologic pathways that underlie the remodeling response after MI remain to be determined. To better define the factors that may be involved in the neovascularization response after MI, our laboratory has recently developed a PET probe that binds to VEGFRs in the living animal (17). We have recently shown, using small-animal tumor models, the feasibility of assessing the presence of VEGFR in normal and disease states (17). The use of noninvasive imaging modalities will permit us, for the first time, to monitor receptor expression in the intact subject.

Thus, we hypothesize that MI will be associated with an increase in the expression of VEGFR and that such expression can be serially monitored using PET.

Materials and Methods

Protocol Design

Protocols were approved by the Stanford Animal Research Committee and conformed with the *Guide for the Care and Use of Laboratory Animals* (18). Animals were divided into 2 groups: sham operated (n = 3) and MI (n = 8). On day −4, animals underwent high-resolution ultrasound for assessment of baseline cardiac function. On day 0, coronary artery ligation was induced in MI animals, whereas control animals where sham operated. Three days after surgery, cardiac function was reevaluated to confirm the presence and to assess the extent of MI. Dedicated small-animal PET (Siemens Medical Solutions, Inc.) imaging was performed on days −4, 3, 10, 17, and 24 after the induction of MI. At different time points, animals were euthanized and tissue was harvested for ex vivo studies (for histology and autoradiography).

Induction of MI

Induction of MI was done as described earlier by our laboratory (19). Adult female Sprague–Dawley rats (weight, 150–200 g; Charles River Laboratories) were used for this study. On the day of surgery, anesthesia was induced with isoflurane (5%) and the animals were intubated for mechanical ventilation. The anesthesia was then maintained with isoflurane (2%). MI was induced by ligation of the left anterior descending coronary artery 2–3 mm from the tip of the left auricle with a 7-0 polypropylene suture. This resulted in myocardial blanching and ST-segment elevation on an electrocardiogram monitor (EC-60 model; Silogic). In the sham-operated animals, a suture was placed in the myocardium (without ligating the left coronary artery).

Assessment of LV Contractility with Echocardiography

Cardiac function was assessed as described (19). Briefly, rats received isofluorane (2%) for general anesthesia and were placed on the scanning table. Echocardiographic images were obtained using a dedicated small-animal high-resolution-imaging unit and a 30-MHz linear transducer (Vevo 770; Visualsonics) (20). Using the parasternal short-axis view, LV end-diastolic and LV end-systolic diameters (LVEDD and LVESD, respectively) were measured, and LV fractional shortening was calculated as = (LVEDD − LVESD)/LVEDD × 100, as described. All measurements were averaged on 3 consecutive cardiac cycles (19).

PET Probe Synthesis

Radiosynthesis of ^{64}Cu-DOTA-VEGF$_{121}$—All commercially available chemical reagents were used without further purification. DOTA (1,4,7,10-tetraazadodecane-N,N′,N″,N‴-tetraacetic acid) was purchased from Macrocyclics, Inc., and Chelex 100 resin (50–100 mesh) was purchased from Aldrich. PD-10 columns were purchased from GE Healthcare. ^{64}Cu was obtained from the University of Wisconsin–Madison.

The detailed procedure for the synthesis of ^{64}Cu-DOTA-VEGF$_{121}$ has been reported earlier (17). DOTA-VEGF$_{121}$ was purified using a PD-10 column and concentrated by Centricon filter units (Ultracel YM-10; Millipore). ^{64}Cu labeling was performed in 0.1 M sodium acetate buffer (NaOAc, pH 6.5) at 40°C using 10 μg of DOTA-VEGF$_{121}$ per 37 MBq (mCi) of ^{64}Cu. The radiolabeling yield of ^{64}Cu-DOTA-VEGF$_{121}$ was 87.4% ± 3.2%, with a specific activity of 3.2 ± 0.1 GBq/mg and a radiochemical purity of >98%. To determine the specificity of this probe for the VEGFR we performed cell-binding assays. The detailed procedure for the cell-binding assay has been reported earlier (17,21,22). Receptor-binding affinity of VEGF$_{121}$ and DOTA-VEGF$_{121}$ was analyzed by the porcine endothelial cells (PAE)/KDR cell-binding assay using ^{125}I-VEGF$_{165}$ as the radioligand. To determine the serum stability, ^{64}Cu-DOTA-VEGF$_{121}$ was incubated with complete rat serum at 37°C for up to 4 h. At different time points, aliquots of the mixture were injected onto an analytic high-performance liquid chromatography (HPLC) system (Vydac protein C4 column 214TP54; flow rate, 1 mL/min). The radioactive peaks of ^{64}Cu and ^{64}Cu-DOTA-VEGF$_{121}$ were each integrated to calculate the percentage of intact tracer.

Radiosynthesis of ^{18}F-FDG—^{18}F-FDG synthesis was performed at the Stanford Cyclotron Unit, as described (23).

Small-Animal PET Scanning

Scanning was done using methods described earlier (19). Animals were anesthetized with isofluorane (2%) and injected with approximately 37 MBq (1 mCi) of ^{64}Cu-DOTA-VEGF$_{121}$ via the tail vein and allowed to recover. To determine the best signal-to-background ratio, animals were scanned at 1, 4, 18, and 24 h after injection of the tracer. At the time of

scanning, animals were anesthesized with isofluorane (2%) and prone positioned on the microPET R4 rodent model scanning gantry (Siemens Medical Solutions, Inc.). The scanner has a computer-controlled bed and 10.8-cm transaxial and 8-cm axial fields of view (FOVs). The voxel size was 0.845 mm on a side, and the full width at half maximum was 1.66, 1.65, and 1.84 mm for tangential, radial, and axial orientations, respectively. The scanner has no septa and operates exclusively in the 3-dimensional list mode. A 15-min static acquisition was performed with the mid thorax in the center of the FOV, and images were reconstructed using a filtered backprojection (FBP) algorithm. Uptake was calculated as the percentage injected dose per gram (%ID/g) of tissue (19,24,25) using the AMIDE software (26). In each scan, 3 different regions of interest (ROIs), 2 mm in diameter, were drawn over the myocardial uptake within the infarcted area, and the mean %ID/g of tissue was averaged. No correction was performed for partial-volume effects. In addition, signal from the infarcted area was compared with the contralateral myocardium (at the septal level), which was taken as background signal, and expressed as the signal-to-background ratio.

To confirm the myocardial origin of the ^{64}Cu-DOTA-VEGF$_{121}$–detected signal, we performed viability studies using ^{18}F-FDG (19,27,28). Immediately after the ^{64}Cu-DOTA-VEGF$_{121}$ scan, animals were kept in the scanning gantry (for image coregistration) and injected with 18.5 MBq (500 μCi) of ^{18}F-FDG (Stanford Cyclotron Unit). One hour after ^{18}F-FDG injection, a 15-min static acquisition was performed with the mid thorax in the center of the FOV, and images were reconstructed using a FBP algorithm (19,24,25).

microCT Scanning

To anatomically localize the tracer signal obtained using PET, animals from both groups were also scanned in a microCT scanner (eXplore RS MicroCT System; GE Healthcare). Immediately after PET, and using fiducial markers for coregistration, animals were transported to the microCT scanning gantry, positioned, and scanned at a voxel resolution of 97 μm (scanning time, 7 min). Images were reconstructed using built-in software (Microview; GE Healthcare). CT and PET datasets were loaded into AMIDE (26), and fiducial markers were coregistered for alignment of datasets.

Validation of VEGF Probe Specificity and Receptor Expression

Mutant Studies—To test the specificity of the ^{64}Cu-DOTA-VEGF$_{121}$, we designed a VEGF$_{mutant}$ that does not bind to VEGFR-2. This VEGF$_{mutant}$ was generated through recombinant DNA technology by mutating the amino acid residues involved in VEGFR binding (29). The amino acid residues at positions 63, 64, 67, 82, 83, and 84 were replaced with alanine. ^{64}Cu-DOTA-VEGF$_{mutant}$ was prepared using the same procedure as that used for ^{64}Cu-DOTA-VEGF$_{121}$. The radiolabeling yield was 93%, with a specific activity of 3.3 ± 0.6 GBq/mg and a radiochemical purity of >98%. The ^{64}Cu-DOTA-VEGF$_{mutant}$ was administered to post-MI rats following the same imaging protocol as that for the experimental and sham-operated group.

Autoradiography—To further confirm that the signal obtained in PET was of myocardial origin, immediately after scanning animals (n = 3 in each group) were euthanized and the heart was harvested (on day 3). Heart samples were frozen on dry ice and 30-μm slices were obtained (Bright 5030/WD/MR cryomicrotome; Hacker Instruments) and exposed for 6–7 h on a Phosphoimager plate (Perkin Elmer), developed in a Cyclone (Perkin Elmer), and read using Optiquant software (Packard Instrument Co.) (17).

VEGFR Immunostaining—Myocardial frozen tissue slices (5-μm thick) were fixed with ice-cold acetone for 10 min and dried in air for 30 min. The slices were rinsed with phosphate-buffered saline for 2 min and blocked with 10% donkey serum for 30 min at room temperature.

The slices were incubated with rabbit antirat VEGFR-2 antibody overnight at 4°C and visualized using Cy3-conjugated donkey antirat secondary antibody (1:200; Jackson ImmunoResearch Laboratories, Inc.). For VEGFR-1 staining, the tissue slices were incubated with rabbit antirat VEGFR-1 antibody (1:50; Lab Vision Corp.) at room temperature for 1 h and visualized with Cy3-conjugated donkey antirabbit secondary antibody (1:200; Jackson ImmunoResearch Laboratories, Inc.) (17). Immunofluorescence was visualized in an Axiovert 200 M microscope (Carl Zeiss) using a Ds-red filter set (excitation, 545 nm; emission, 620 nm).

Statistical Analysis

Data are expressed as mean ± SEM. Statistical analysis used the unpaired Student *t* test with unequal variance (for comparison between sham-operated and MI animals) and the paired Student *t* test for comparison before and after MI. A P value < 0.05 was considered statistically significant.

Results

General Characteristics/Assessment of Cardiac Function

There was no difference in weight or heart rate between sham ($n = 3$) and MI ($n = 8$) animals. At baseline (day: −4), animals from both groups had similar myocardial cardiac function, as assessed by fractional shortening ($P = 0.17$; Table 1). In the experimental group, MI induction led to a defect in ^{18}F-FDG uptake, as assessed by PET (Fig. 1B, white arrow) and akinesis of the anterolateral wall with a significant decrease in cardiac function (assessed by M-mode high-resolution ultrasound on day 10 postoperatively; Fig. 1D and Table 1). On the other side, in sham-operated animals, there was no uptake defect in ^{18}F-FDG PET (Fig. 1A), and cardiac function remained stable compared with baseline ($P = 0.13$; Fig. 1C and Table 1). The MI procedure had a mortality of 15%, similar to that reported by other investigators (19).

Radiolabeling of ^{64}Cu-DOTA-VEGF$_{121}$ and ^{64}Cu-DOTA-VEGF$_{mutant}$

^{64}Cu-DOTA-VEGF$_{121}$ was stable in rat serum, having at least 75% stability 1 h after incubation in rat serum and remaining stable for 4 h, with 3%–5% free ^{64}Cu, and the rest (20%) was composed of partial compound and metabolites. The binding of VEGF$_{121}$ and DOTA-VEGF$_{121}$ to endothelial cells expressing VEGFR-2 was assessed using ^{125}I-VEGF$_{165}$ as the radioligand. The 50% inhibitory concentration (IC_{50}) values were 1.11 and 1.59 nmol/L for VEGF$_{121}$ and DOTA-VEGF$_{121}$, respectively. The IC_{50} values for VEGF$_{121}$ and VEGF$_{mutant}$ to PAE transfected with VEGFR-1 were 5.4 and 11.3 nmol/L, respectively. The IC_{50} for VEGF$_{121}$ to PAE-VEGFR-2 cells was 1.5 nmol/L, whereas the IC_{50} for the VEGF$_{mutant}$ was in excess of 10 μmol/L. These data show that the VEGF$_{mutant}$ does not bind to VEGFR-2 and only partially binds to VEGFR-1, providing evidence of the specificity of the experimental probe used in this study (^{64}Cu-DOTA-VEGF$_{121}$).

Assessment of Myocardial VEGFR Expression in Living Rats

To localize the anatomic region of the ^{64}Cu-DOTA-VEGF$_{121}$ PET–detected signal, we performed microCT on MI animals. The top left panel of Figure 2 shows the microCT image, anatomically separating the myocardium from the chest wall, whereas the top right image shows a representative image of the ^{64}Cu-DOTA-VEGF$_{121}$ PET image from the same animal (day 3 after MI). In the top center panel, the fused image clearly demonstrates the myocardial origin of the ^{64}Cu-DOTA-VEGF$_{121}$ signal.

As mentioned earlier, in MI animals ^{18}F-FDG (for assessment of myocardial viability; Fig. 2, bottom left) was injected immediately after the ^{64}Cu-DOTA-VEGF$_{121}$ scan (Fig. 2, bottom

right). ^{18}F-FDG and ^{64}Cu-DOTA-VEGF$_{121}$ images were fused (Fig. 2, bottom center) showing that the ^{64}Cu-DOTA-VEGF$_{121}$ myocardial signal matched extremely well with the areas of infarcted myocardium, as evidenced by a lack of ^{18}F-FDG uptake. On the other hand, in sham-operated animals, there were no infarcted areas, and thus no lack of ^{18}F-FDG uptake (Fig. 1A). Furthermore, postoperatively, animals (both sham and MI groups) had increased uptake of ^{18}F-FDG at the level of the surgical wound (Figs. 1A and 1B and Fig. 2, arrowheads), consistent with an inflammatory response.

The best ^{64}Cu-DOTA-VEGF$_{121}$ signal-to-background ratio was obtained 1 h after injection of the tracer and, thus, was used for signal quantification and analysis in this study (1 h, 2.60 ± 0.30; 4 h, 2.43 ± 0.46; no consistent signal could be detected at the 18- and 24-h scans). The top panel of Figure 3 shows representative images of baseline (left, 4 d before MI) with minimal probe uptake and MI animals (middle, left) with probe uptake in the chest wall (white arrowhead), but most importantly, a clearly distinct signal, representing myocardial probe uptake (red arrow). In sham-operated animals (middle, right), the white arrowhead shows probe uptake only at the level of the chest wall-product of the open thoracotomy procedure. The right panel shows a representative VEGF$_{mutant}$ scan with minimal uptake of the probe. The middle panel of Figure 3 shows representative images of the uptake of ^{64}Cu-DOTA-VEGF$_{121}$ over time, illustrating the increase in uptake on day 3 after MI and the decrease in probe uptake over time. The bottom panel of Figure 3 shows the quantitative analysis from all groups. On day −4 (before MI induction or sham operation), there was no significant myocardial uptake of ^{64}Cu-DOTA-VEGF$_{121}$ (0.30 ± 0.07 %ID/g; Fig. 3, top left). MI induction was associated with a significant increase in uptake of ^{64}Cu-DOTA-VEGF$_{121}$ in the anterolateral wall of the myocardium (MI, 0.97 ± 0.05 %ID/g; $P < 0.05$ compared with baseline, Fig. 3). ^{64}Cu-DOTA-VEGF$_{121}$ uptake after MI was also significantly different compared with sham ($P = 0.01$, both on day 3 after intervention) and VEGF$_{mutant}$ ($P = 0.001$). Similarly to ^{18}F-FDG, animals from both groups had a comparable increase in uptake of ^{64}Cu-DOTA-VEGF$_{121}$ at the level of the surgical wound (Fig. 3 top panel, white arrowhead), probably reflecting an angiogenic response during the wound healing process (sham, 1.00 ± 0.12 %ID/g; MI, 1.03 ± 0.06 %ID/g; $P = 0.39$).

In summary, the PET ^{64}Cu-DOTA-VEGF$_{121}$ myocardial uptake was higher on day 3 postoperatively and decreased over time until it reached baseline levels on day 24 (Fig. 3, bottom). Importantly, the increased tracer uptake was seen only in the areas supplied by the ligated coronary artery and not in remote areas.

Validation of VEGF Specificity and Receptor Expression

VEGF Probe Specificity—MI was induced in 4 animals using the approach described earlier and animals imaged on day 10 after MI with the ^{64}Cu-DOTA-VEGF$_{mutant}$. The uptake in the myocardial infarct zone (0.098 ± 0.008 %ID/g) or muscular chest wall was significantly lower than that of ^{64}Cu-DOTA-VEGF$_{121}$ at a comparable day after MI (0.78 ± 0.06 %ID/g, $P < 0.05$; Fig. 3, bottom panel). Such observation provides direct and critical evidence that the ^{64}Cu-DOTA-VEGF$_{121}$ is specific for the VEGFR.

Autoradiography—Autoradiography of the explanted hearts after ^{64}Cu-DOTA-VEGF$_{121}$ PET clearly shows that the increase in signal observed with PET comes from the affected myocardium, as evidenced by increased activity in the anterolateral (AL) wall compared with the contralateral (CL) wall (MI: AL/CL wall, 5.24 ± 0.31; Fig. 4A, right). On the contrary, sham-operated animals had no difference in activity between the 2 regions (sham: AL/CL wall, 1.14 ± 0.02; Fig. 4A, left). These results show that the uptake observed is due to true tissue uptake rather than an artifact from changes in contractility of the LV.

VEGFR Immunostaining—To further characterize the activation of the VEGFRs after MI, we performed immunofluorescence staining of myocardial tissue slices for VEGFR-1 and VEGFR-2 and observed an increase in the expression of VEGFR-1 and VEGFR-2 after MI compared with sham operation (Fig. 4B). Importantly, the expression of VEGFRs was more pronounced on day 3 and decreased over time (Fig. 4B), following a similar trend to what is seen with noninvasive PET imaging.

Discussion

In the current study we imaged and described, in living subjects, the kinetics of VEGFRs in a rat model of MI. Use of noninvasive imaging strategies, such as the one presented here, that permit the study of biologic pathways in living subjects can provide invaluable in vivo information with regard to the pathobiology of CAD and, because of its noninvasive nature, has the potential to be translated to patients.

Several issues should be addressed with regard to the approach we used in this study. ^{64}Cu has a relatively long half-life ($t_{1/2}$ = 12.7 h), which precluded us from performing more frequent monitoring of VEGFR expression. In addition, the use of radioactive isotopes with a relatively long half-life is less translatable to patients. On the basis of the results of this study (the best signal-to-background ratio was obtained 1 h after probe delivery), future studies will likely benefit by using radioisotopes with shorter half-lives, such as ^{18}F ($t_{1/2}$ = 109 min) or ^{68}Ga ($t_{1/2}$ = 68 min). In that respect, either ^{68}Ga or ^{18}F will be a potential alternative as their half-lives are sufficiently short to provide reasonably low radiation exposure but long enough to allow for radio-labeling of $VEGF_{121}$.

To image VEGFRs in this study, we used the $VEGF_{121}$ protein as the substrate for the VEGFR. Previous studies have shown that $VEGF_{121}$ has high affinity for both VEGFR-1 and VEGFR-2. Thus, on the basis of the in vivo results from this study we cannot conclude whether there is differential activation of VEGFRs after MI. Furthermore, it is also possible that part of the increased uptake observed after MI is due to an inflammatory response, which is a known response to MI (30,31). The intact fraction of ^{64}Cu-DOTA-$VEGF_{121}$ after incubation with rat serum is at least 75%, based on analytic HPLC, with a very small fraction (3%–5%) of free ^{64}Cu. The remaining fraction (20%) was composed of metabolites and fragments of the tracer. Although they can possibly be taken up by inflammation, which may contribute to a certain fraction of the uptake in the infarct region, the majority will likely be cleared very rapidly on our previous studies using ^{64}Cu-labeled small peptides (32). In addition, our in vivo mutant studies support the concept that the majority of the signal observed is due to the upregulation of VEGFRs and not to other issues, such as vascular protein leakage in a state of inflammation. Furthermore, it is important to note that changes in LV contractility between animals from different groups could act as a confounding variable in the analysis and should be taken into consideration when analyzing the results of this study. However, our ex vivo studies (in which LV contractility does not play a role in the observed uptake) using ^{125}I-VEGF as the detection probe provide evidence of the myocardial location of the detected signal. In vivo mutant studies also demonstrate that the signal detected in MI rats was not due to factors such as increased in vivo regional perfusion but, rather, to an actual increase in the expression of the VEGFRs. Moreover, the increased expression in VEGFRs observed with immunohistochemistry in the myocardial infarcted areas also provides indirect evidence of the upregulation of VEGFRs in MI, with a decrease over time to levels that do not differ from baseline. However, note that, whereas immunohistochemistry is a qualitative methodology used for localization, the in vivo PET data are quantitative and, therefore, should be taken as a better assessment of the VEGFR expression in the myocardium after MI. Our observation corroborates the observations made by Li et al., who described a dynamic and differential activation of VEGFRs after MI (1). It should also be mentioned that no partial-volume

correction was done in this proof-of-principle study; thus, its results should not be taken as absolute quantification but, rather, as proof of the increased expression of VEGFR after MI.

The present study used a rat model of MI, with permanent ligation of a coronary artery (19). We chose this model of disease because it allows us to study the remodeling effect that infarction has on the myocardium, without confounding variables (e.g., such as reperfusion injury) that may be observed with variants of this model (transient coronary ligation followed by reperfusion) (33). However, although the permanent ligation animal model (1,19) is commonly used as a surrogate of CAD and MI seen in patients, it may not resemble the actual disease observed in humans. Thus, results from this study should not be extrapolated directly to what occurs in patients but seen, rather, as a first and necessary step toward developing novel imaging modalities that will lead to a better understanding of CAD. Future studies from our laboratory will focus on the translation of this imaging approach to a larger animal model (e.g., porcine) as a preamble for its use in patients. To our knowledge, this imaging approach will be the first one to allow investigation of the expression of growth factor receptors in large animals and then in patients in a noninvasive and longitudinal manner. The understanding of the pathobiology of CAD in patients is critical for the development of novel therapeutic strategies and to better define the role of those that are currently available. Specifically, imaging of the VEGFR has the potential to be used to accurately study the time line of the activation of growth factors in the intact patient during different stages of the disease (diagnosis/prognosis) as well as provide insight on the effects of different therapeutic strategies (e.g., gene/cell therapy).

Conclusion

We imaged and described the kinetics of ^{64}Cu-DOTA-VEGF$_{121}$ uptake in a rat model of MI. Use of molecular imaging strategies to study the biology of CAD and its consequences will be invaluable in providing information on the activation of different biologic pathways and, because of its potential application to patients, will help us to better understand CAD.

Acknowledgments

This research was supported in part by the Mayo Clinical Scholarship (Mayo Clinic College of Medicine, Rochester, MN) and by the Benedict Cassen Postdoctoral Fellowship (Education and Research Foundation for the Society of Nuclear Medicine). This work was also supported in part by grants NCI SAIRP, NHLBI 1 R01 HL078632, and NCI ICMIC CA114747 P50; The Clayton Foundation for Research; and grants NCI R21 CA102123, NIBIB R21 EB001785, DOD W81XWH-04-1-0697, W81XWH-06-1-0665, W81XWH-06-1-0042, and DAMD17-03-1-0143. We also thank the cyclotron team at the University of Wisconsin–Madison for ^{64}Cu production and the Stanford cyclotron team (David Dick and Fred Chin) for ^{18}F-FDG production.

References

1. Li J, Brown LF, Hibberd MG, Grossman JD, Morgan JP, Simons M. VEGF, flk-1, and flt-1 expression in a rat myocardial infarction model of angiogenesis. Am J Physiol 1996;270:H1803–H1811. [PubMed: 8928889]
2. Lee SH, Wolf PL, Escudero R, Deutsch R, Jamieson SW, Thistlethwaite PA. Early expression of angiogenesis factors in acute myocardial ischemia and infarction. N Engl J Med 2000;342:626–633. [PubMed: 10699162]
3. Ferrara N. The role of VEGF in the regulation of physiological and pathological angiogenesis. EXS 2005:200–231.
4. McColl BK, Stacker SA, Achen MG. Molecular regulation of the VEGF family: inducers of angiogenesis and lymphangiogenesis. APMIS 2004;112:463–480. [PubMed: 15563310]
5. McMahon G. VEGF receptor signaling in tumor angiogenesis. Oncologist 2000;5(suppl 1):3–10. [PubMed: 10804084]

6. Goodsell DS. The molecular perspective: VEGF and angiogenesis. Oncologist 2002;7:569–570. [PubMed: 12490744]
7. LeCouter J, Lin R, Ferrara N. The role of EG-VEGF in the regulation of angiogenesis in endocrine glands. Cold Spring Harb Symp Quant Biol 2002;67:217–221. [PubMed: 12858543]
8. Carmeliet P. VEGF as a key mediator of angiogenesis in cancer. Oncology 2005;69(suppl 3):4–10. [PubMed: 16301830]
9. Shinohara K, Shinohara T, Mochizuki N, et al. Expression of vascular endothelial growth factor in human myocardial infarction. Heart Vessels 1996;11:113–122. [PubMed: 8897060]
10. Wu JC, Tseng JR, Gambhir SS. Molecular imaging of cardiovascular gene products. J Nucl Cardiol 2004;11:491–505. [PubMed: 15295418]
11. Herschman HR, MacLaren DC, Iyer M, et al. Seeing is believing: non-invasive, quantitative and repetitive imaging of reporter gene expression in living animals, using positron emission tomography. J Neurosci Res 2000;59:699–705. [PubMed: 10700006]
12. Massoud TF, Gambhir SS. Molecular imaging in living subjects: seeing fundamental biological processes in a new light. Genes Dev 2003;17:545–580. [PubMed: 12629038]
13. Su H, Spinale FG, Dobrucki LW, et al. Noninvasive targeted imaging of matrix metalloproteinase activation in a murine model of postinfarction remodeling. Circulation 2005;112:3157–3167. [PubMed: 16275862]
14. Chen J, Tung CH, Allport JR, Chen S, Weissleder R, Huang PL. Near-infrared fluorescent imaging of matrix metalloproteinase activity after myocardial infarction. Circulation 2005;111:1800–1805. [PubMed: 15809374]
15. Meoli DF, Sadeghi MM, Krassilnikova S, et al. Noninvasive imaging of myocardial angiogenesis following experimental myocardial infarction. J Clin Invest 2004;113:1684–1691. [PubMed: 15199403]
16. Lu E, Wagner WR, Schellenberger U, et al. Targeted in vivo labeling of receptors for vascular endothelial growth factor: approach to identification of ischemic tissue. Circulation 2003;108:97–103. [PubMed: 12821549]
17. Cai W, Chen K, Mohamedali KA, et al. PET of vascular endothelial growth factor receptor expression. J Nucl Med 2006;47:2048–2056. [PubMed: 17138749]
18. National Institutes of Health. Guide for the Care and Use of Laboratory Animals. 1996 [February 17, 2008]. Available at: http://www.nap.edu/catalog.php?record_id55140
19. Wu JC, Chen IY, Wang Y, et al. Molecular imaging of the kinetics of vascular endothelial growth factor gene expression in ischemic myocardium. Circulation 2004;110:685–691. [PubMed: 15302807]
20. Rodriguez-Porcel M, Gheysens O, Chen IY, Wu JC, Gambhir SS. Image-guided cardiac cell delivery using high-resolution small-animal ultrasound. Mol Ther 2005;12:1142–1147. [PubMed: 16111921]
21. Chen X, Plasencia C, Hou Y, Neamati N. Synthesis and biological evaluation of dimeric RGD peptide-paclitaxel conjugate as a model for integrin-targeted drug delivery. J Med Chem 2005;48:1098–1106. [PubMed: 15715477]
22. Zhang X, Xiong Z, Wu Y, et al. Quantitative PET imaging of tumor integrin $\alpha_V\beta_3$ expression with ^{18}F-FRGD2. J Nucl Med 2006;47:113–121. [PubMed: 16391195]
23. Lemaire C, Damhaut P, Lauricella B, et al. Fast [^{18}F]FDG synthesis by alkaline hydrolysis on a low polarity solid phase support. J Labelled Compds Radiopharm 2002;45:435–447.
24. Wu JC, Chen IY, Sundaresan G, et al. Molecular imaging of cardiac cell transplantation in living animals using optical bioluminescence and positron emission tomography. Circulation 2003;108:1302–1305. [PubMed: 12963637]
25. Su H, Forbes A, Gambhir SS, Braun J. Quantitation of cell number by a positron emission tomography reporter gene strategy. Mol Imaging Biol 2004;6:139–148. [PubMed: 15193248]
26. Loening AM, Gambhir SS. AMIDE: a free software tool for multimodality medical image analysis. Mol Imaging 2003;2:131–137. [PubMed: 14649056]
27. Schroter G, Schneider-Eicke J, Schwaiger M. Assessment of tissue viability with fluorine-18-fluoro-2-deoxyglucose (FDG) and carbon-11-acetate PET imaging. Herz 1994;19:42–50. [PubMed: 8150413]

28. Ghesani M, Depuey EG, Rozanski A. Role of F-18 FDG positron emission tomography (PET) in the assessment of myocardial viability. Echocardiography 2005;22:165–177. [PubMed: 15693785]

29. Wang H, Cai W, Chen K, et al. A new PET tracer specific for vascular endothelial growth factor receptor 2. Eur J Nucl Med Mol Imaging 2007;34:2001–2010. [PubMed: 17694307]

30. Ren G, Dewald O, Frangogiannis NG. Inflammatory mechanisms in myocardial infarction. Curr Drug Targets Inflamm Allergy 2003;2:242–256. [PubMed: 14561159]

31. Nian M, Lee P, Khaper N, Liu P. Inflammatory cytokines and postmyocardial infarction remodeling. Circ Res 2004;94:1543–1553. [PubMed: 15217919]

32. Wu Y, Zhang X, Xiong Z, et al. microPET imaging of glioma integrin $\alpha_v\beta_3$ expression using ^{64}Cu-labeled tetrameric RGD peptide. J Nucl Med 2005;46:1707–1718. [PubMed: 16204722]

33. Thim T, Bentzon JF, Kristiansen SB, et al. Size of myocardial infarction induced by ischaemia/reperfusion is unaltered in rats with metabolic syndrome. Clin Sci (Lond) 2006;110:665–671. [PubMed: 16448385]

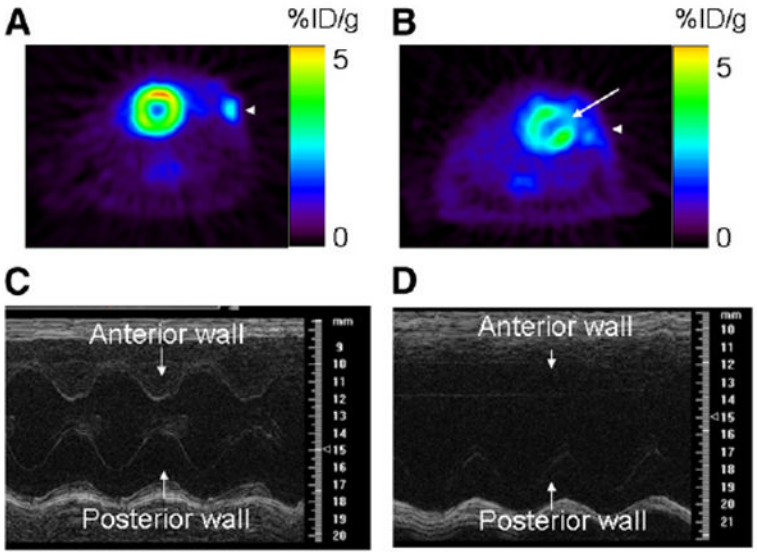

FIGURE 1.

Cardiac functional assessment using ^{18}F-FDG PET and high-resolution ultrasound (at frequency of 30 MHz). (Top) ^{18}F-FDG PET of sham-operated animal (A) and animal after MI (B). Sham operation did not induce any ^{18}F-FDG defect, whereas MI was associated with medium-sized defect in anterolateral wall (white arrow). (Bottom) M-mode ultrasound at midventricle level in sham-operated animal (C) and animal after MI (D). After MI, there was akinesis of anterolateral wall and significant decrease in fractional shortening compared with that of sham-operated animals.

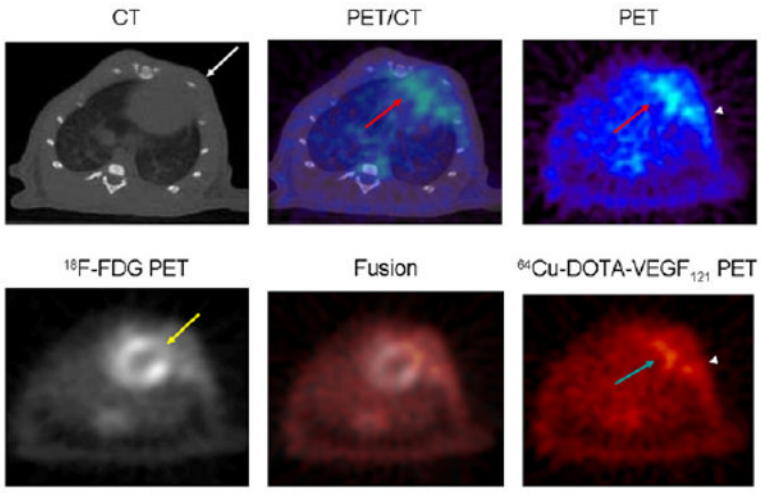

FIGURE 2.

Myocardial origin of ^{64}Cu-DOTA-VEGF$_{121}$ PET signal after MI. (Top) Representative coregistered images of microCT (left), PET (right), and fused PET/CT image (center) in MI animal clearly demonstrates that the ^{64}Cu-DOTA-VEGF$_{121}$ signal detected with PET corresponds to anterolateral myocardium (PET and fused images, red arrow) and clearly separated from intercostal muscle layer (microCT image, white arrow). There is also increased uptake in area of surgical wound (PET image, arrowhead). (Bottom) Representative images of ^{64}Cu-DOTA-VEGF$_{121}$ (left), ^{18}F-FDG (right), and ^{64}Cu-DOTA-VEGF$_{121}$/^{18}F-FDG fused image (middle). ^{18}F-FDG scan shows that coronary artery ligation resulted in lack of ^{18}F-FDG uptake (yellow arrow) and that uptake of ^{64}Cu-DOTA-VEGF$_{121}$ occurs in areas supplied by ligated coronary artery (turquoise arrow). Fusion of both scans results in complementation of ^{18}F-FDG and ^{64}Cu-DOTA-VEGF$_{121}$ signals. There is also increased uptake in area of surgical wound (arrowhead).

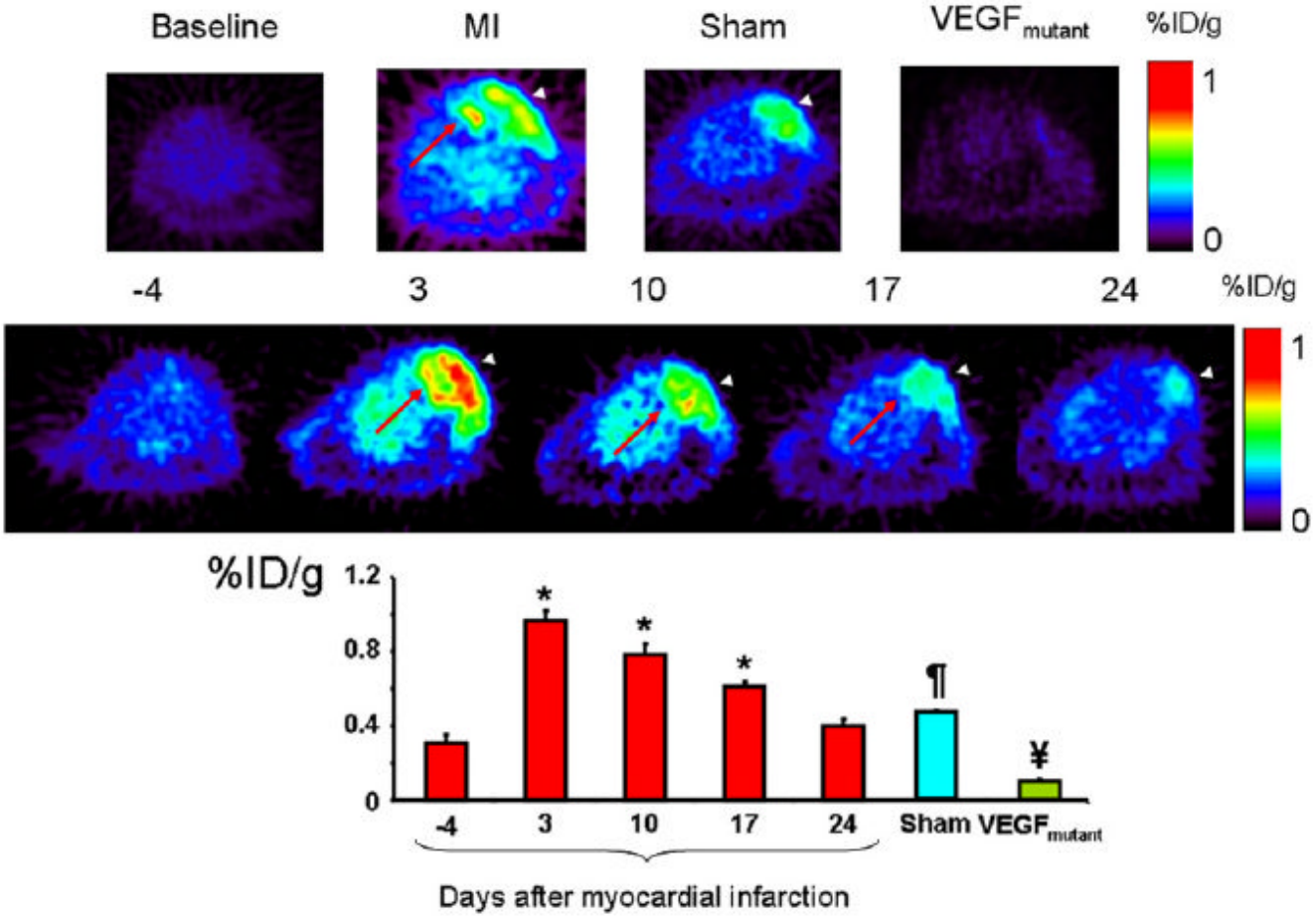

FIGURE 3.

(Top) Representative images at baseline (left), animals after MI (middle left), and sham-operated animals (middle right) show difference in myocardial uptake in MI animals compared with baseline and sham animals. Red arrow shows the ^{64}Cu-DOTA-VEGF$_{121}$ signal from myocardium (seen only in MI animals), and arrowheads show ^{64}Cu-DOTA-VEGF$_{121}$ signal from the surgical wound (muscle layer), which is present in both sham-operated and MI animals. Right panel shows typical image acquired using VEGF$_{mutant}$, with minimal uptake, supporting the specificity of ^{64}Cu-DOTA-VEGF$_{121}$ probe for VEGFRs. (Middle) Representative images correspond to 1 animal of MI group illustrating uptake of ^{64}Cu-DOTA-VEGF$_{121}$ over time (in days after induction of MI), clearly showing time-dependent effect on uptake of ^{64}Cu-DOTA-VEGF$_{121}$. Red arrow points to myocardial upake, whereas white arrowhead points to chest wall muscular layer uptake. (Bottom) Quantification of ^{64}Cu-DOTA-VEGF$_{121}$ after MI over time, expressed in %ID/g of tissue. ^{64}Cu-DOTA-VEGF$_{121}$ uptake was highest on day 3 postoperatively (compared with baseline, day −4) and continues to be elevated until day 17 postoperatively. ^{64}Cu-DOTA-VEGF$_{121}$ uptake was also significantly different compared with sham-operated animals and VEGF$_{mutant}$. *$P < 0.05$ compared with baseline; $^{¥}P < 0.05$ compared with sham and ^{64}Cu-DOTA-VEGF$_{121}$; $^{¶}P < 0.05$ compared with VEGF$_{mutant}$ and ^{64}Cu-DOTA-VEGF$_{121}$.

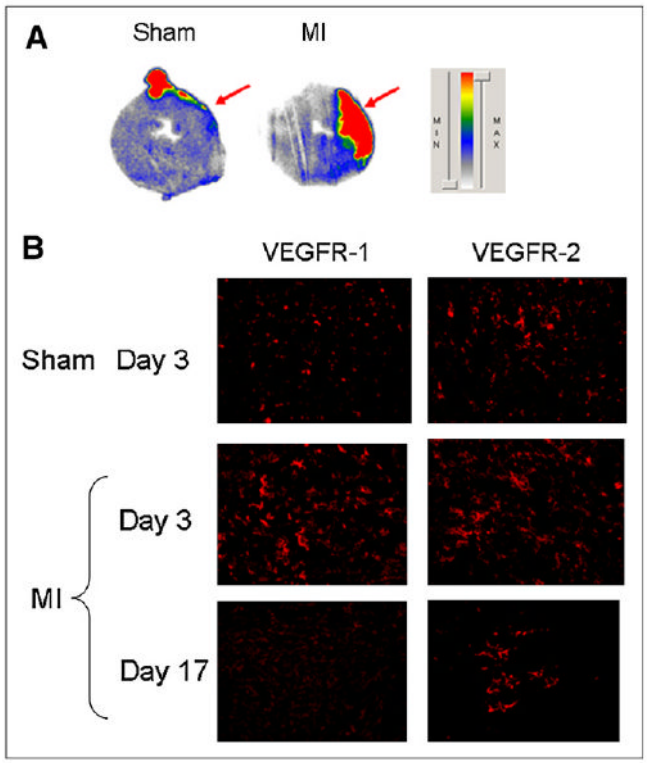

FIGURE 4.

Ex vivo studies. (A) Autoradiography of 30-μm myocardial slices of both sham-operated (left) and MI (right) animals after injection of ^{64}Cu-DOTA-VEGF$_{121}$ shows increased signal in anterolateral wall of LV of MI animals, whereas no activity is detected in sham group. Red arrows point to area affected by ligated artery (anterolateral wall), clearly showing the myocardial origin of signal observed. (B) Immunofluorescence staining for VEGFR-1 (left) and VEGFR-2 (right) in sham-operated and MI animals (on days 3 and 17 after MI). MI is associated with marked increase in VEGFR-1 and VEGFR-2 immunostaining, which was higher than that of sham animals. VEGFR expression is higher on day 3 and diminishes over time, similar to what it is observed with PET. MIN = minimum; MAX = maximum.

TABLE 1

General Group Characteristics at Both Baseline and After Intervention (Either Sham Operation or MI)

Parameter	Sham	MI
General characteristics		
Weight (g)	184 ± 7	182 ± 9
Heart rate (bpm)	323 ± 20	330 ± 15
Cardiac function parameters		
Baseline		
LVEDD (mm)	61.4 ± 0.8	62.5 ± 1.9
LVEDSD (mm)	30.4 ± 1.7	28.7 ± 5.0
LV FS (%)	50.4 ± 3.5	54.1 ± 5.9
Postoperatively		
LVEDD (mm)	62.5 ± 1.9	72.0 ± 6.5
LVESD (mm)	32.4 ± 2.8	56.8 ± 4.5
LV FS (%)	47.8 ± 2.8	20.7 ± 3.4*

*$P = 0.003$ compared with sham.

LVEDD = left ventricular end-diastolic diameter; LVESD = left ventricular end-systolic diameter; LV FS = left ventricular fractional shortening.

There was no difference in weight, heart rate, or baseline parameters of cardiac function. After MI, there was a decrease in cardiac function, as evidenced by a decrease in fractional shortening, whereas in sham animals cardiac function was preserved.